NANO LETTERS

Letter

pubs.acs.org/NanoLett

Integrated All-Optical Infrared Switchable Plasmonic Quantum Cascade Laser

John Kohoutek, Alireza Bonakdar, Ryan Gelfand, Dibyendu Dey, Iman Hassani Nia, Vala Fathipour, Omer Gokalp Memis, and Hooman Mohseni*

Bio-Inspired Sensors and Optoelectronics Laboratory (BISOL), EECS, Northwestern University, 2145 Sheridan Rd., Evanston, Illinois 60208, United States

ABSTRACT: We report a type of infrared switchable plasmonic quantum cascade laser, in which far field light in the midwave infrared (MWIR, 6.1 μm) is modulated by a near field interaction of light in the telecommunications wavelength (1.55 μm). To achieve this all-optical switch, we used cross-polarized bowtie antennas and a centrally located germanium nanoslab. The bowtie antenna squeezes the short wavelength light into the gap region, where the germanium is placed. The perturbation of refractive index of the germanium due to the free carrier absorption produced by short wavelength light changes the optical response of the antenna and the entire laser intensity at 6.1 μm significantly. This device shows a viable method to modulate the far field of a laser through a near field interaction.

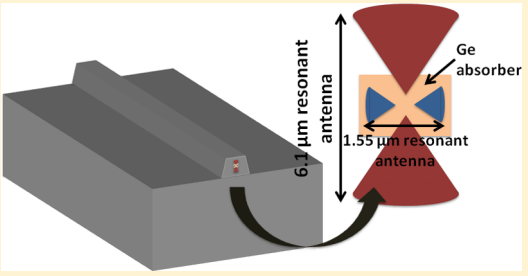

KEYWORDS: *Nanoantenna, all-optical switch, plasmonics, QCL, terahertz, infrared, strong coupling*

Light has been known to generate surface plasmons (SPs) at the interface between two mediums which have opposite signs of dielectric susceptibility (usually metal and dielectric).[1] SPs are collective motions of electrons which can be bound together with evanescent modes in the dielectric. These surface plasmons exhibit resonances which enhance near field amplitude at the resonance wavelength. By coupling two metallic nanoparticles, one can make an antenna with a very high optical amplitude and energy density within a characteristic "hotspot".[2] The antenna material, shape, and geometry can be tuned to maximize the performance for a particular wavelength.[3] Furthermore, because of the enhanced field amplitude, effects that depend on the amplitude such as nonlinear free carrier absorption can also be enhanced by SPs.[4]

The principle of surface plasmons (SPs) has been exploited in many areas, including enhanced optical transmission,[5,6] biosensing,[7,8] and even optical force.[9,10] Recently, there has been increasing activity in using surface plasmon-based devices for optical modulation and switching.[11−13] The modulation of integrated optical signals (i.e., diode lasers) is generally achieved by directly modulating the current that drives the light source. However, all optical modulation methods have become more attractive for applications in compact optical circuits and integrated communication devices. Dionne et al. have used a silicon-based metal−dielectric−metal channel with subwavelength slits for optical source and drain to create an SP-based optical modulator.[11] Pala and colleagues have coupled SPs into and out of a grating and along their path have modulated the signal using a polymer loaded with photochromic molecules.[12] Theoretical work shows that ultrafast and compact all-optical switches can be realized by means of a semiconductor gap-loaded nanoantenna.[13]

With the invention of the quantum cascade laser (QCL),[14] a unipolar semiconductor laser that works on the principle of intersubband transitions, there now exists a compact semiconductor-based laser source in the mid- to far-infrared. Because of the high sensitivity of the cavity mode to the reflectivity of the facets,[15] changing the optical mode properties by externally manipulating the properties at one of the facets is a very attractive way to build an externally modulated light source.

There has also been recent increased interest in making plasmonic devices integrated with quantum-cascade lasers (QCLs).[16−19] Some of these devices may be used for biosensing,[18,19] as many important molecules have vibrational resonance in the terahertz;[20] in addition, plasmonic integrated QCL devices can be used for laser beamshaping or steering.[21] Here we present an antenna-integrated QCL which can be actively and optically modulated using light in the telecommunications wavelength.

We chose two cross-polarized bowtie antennas with an aligned central region for the antenna design. The antenna is placed on the front facet of the QCL so that we may focus the 1550 nm switch beam on the antenna and record the 6.1 μm signal out of the back facet of the laser (see Figure 2). We have chosen bowties over previous designs[18,19] because bowties resonate over a larger spectral range and offer an empty central region where we may place a photonic absorber. The larger bowtie antenna is resonant with the QCL at 6.1 μm wavelength with a length of 1.5 μm per arm and is aligned perpendicular to

Received: February 22, 2012
Revised: March 27, 2012

dx.doi.org/10.1021/nl3007424 | *Nano Lett.* XXXX, XXX, XXX−XXX

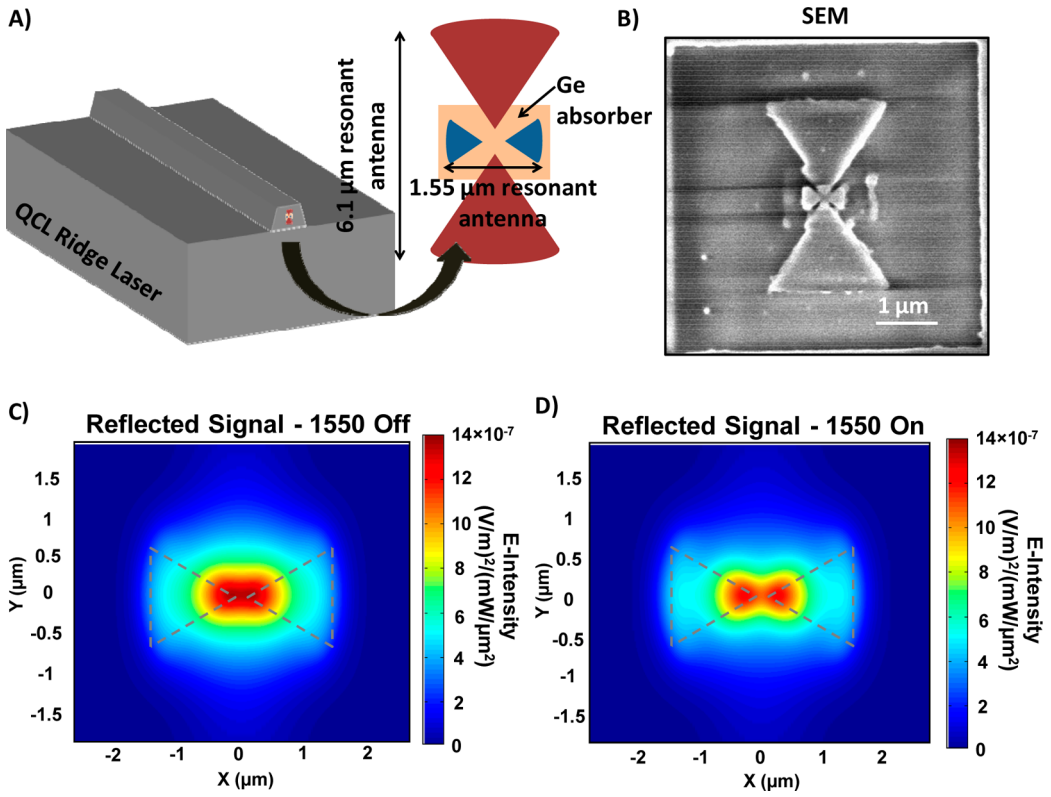

Figure 1. (A) Device schematic (not to scale). (B) Scanning electron micrograph (SEM) showing completed device. (C) Simulated reflected E-intensity signal near the antenna when 1550 nm probe signal is turned off. (D) Simulated reflected E-intensity signal near the antenna when 1550 nm probe signal is turned on. There is a noticeable change in the radiation pattern as well as the peak magnitude of the E-field intensity.

the active region of the device; as the QCL emits TM polarized light, the electric field is aligned with the long axis of the larger bowtie. The smaller bowtie is resonant with the incoming modulating light at 1550 nm with a length of ~200 nm per arm and is aligned perpendicular to the first bowtie. There is a rectangular region (500 nm long, 250 nm wide, and 80 nm tall) of amorphous germanium below the smaller bowtie which acts as an absorber at 1550 nm. The bowties are made out of a single layer of aluminum so as to avoid metal diffusion into the germanium layer below the smaller bowtie antenna. There is a buffer layer of 100 nm of MgF_2 below the entire structure to insulate the top and bottom contacts of the laser as well as protect the facet of the laser. Because the larger bowtie is resonant at 6.1 μm, when the 1550 nm light source is off, there is a high intensity of 6.1 μm light at the center of the larger bowtie. When light at 1550 nm is incident upon the device, it is focused and the intensity is enhanced by the smaller bowtie, creating a large absorption in the small volume of germanium. As a result, free carriers are generated inside the germanium, and it becomes lossy. The free charge dampens the electric field in the germanium, which is in the center of the larger bowtie and is where the largest change in field intensity is observed in the simulations (see Figure 1c,d). Because the antenna is strongly coupled to the cavity modes of the laser, the overall power of the laser is affected significantly.

To analyze and optimize the performance of our design, we simulated the structure using three-dimensional finite-difference time-domain (FDTD) software. All material data used in the simulation, other than the laser region, are from ref 22. The effective refractive index of the laser material is chosen to be 3.2.[18,19] For all simulations, a truncated plane wave is used. Since the smaller bowtie antenna has an area of $\sim \lambda^2/10$, the Gaussian beam from the experiment can be accurately approximated by this uniform plane wave. In addition, the strong interaction between the optical signal at 1550 nm and the structure also happens at the central area of the Gaussian beam due to the alignment of the laser source and the antenna structure. Therefore, the profile of the beam away from the antenna would not impose a significant effect on the absorption process inside the germanium. A TM-polarized source is used to simulate the QCL optical mode to find the resonant length of the larger bowtie antenna, and a TE-polarized source is used to find the resonance length of the smaller antenna. To optimize the design, first, the resonance length of the smaller antenna is found in the absence of the larger antenna. Then, the resonance length of larger antenna is found in the presence of the smaller antenna with the previously obtained resonance length. Finally, the resonance length of smaller antenna is found in the presence of larger antenna with the previously obtained resonance length. A volume monitor is placed in the common gap region of the antennae in order to calculate the average electric field intensity (E-intensity) as a function of arm length. PML boundary conditions are used for all the simulations. In order to find the optically induced plasma in the Ge slab, we have simulated the power absorption in the Ge for a given source intensity at 1.55 μm. Using the Drude model, the free carrier concentration and subsequently the refractive index of Ge at 6.1 μm wavelength are obtained as a function of 1.55 μm wavelength input optical power. Using the modified refractive index, the depth of modulation which is defined as the ratio of power reflectivity of the QCL when the modulator signal is turned on to when the modulator signal is turned off is

dx.doi.org/10.1021/nl3007424 | Nano Lett. XXXX, XXX, XXX−XXX

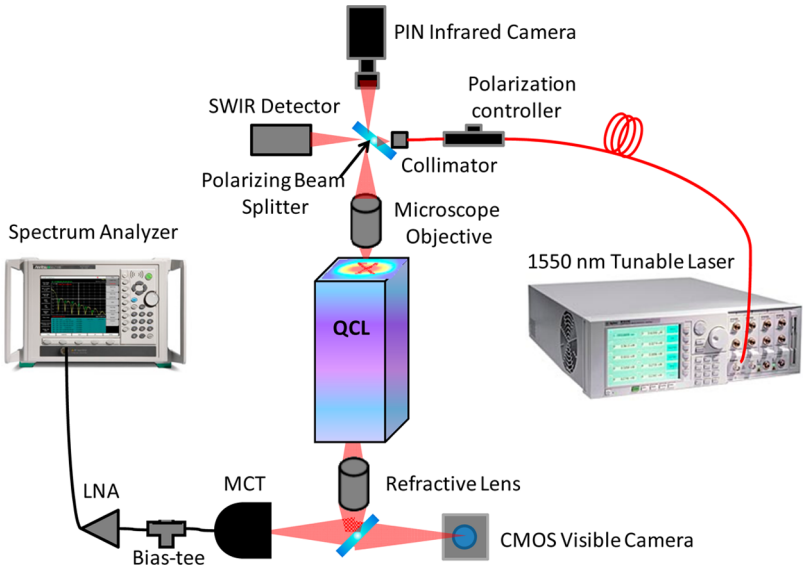

Figure 2. Schematic diagram of experimental setup. There is an NIR camera allowing one to view the top QCL laser facet as well as simultaneously focus the modulation (1550 nm wavelength) laser light onto the laser facet. There is a broadband inverted microscope coupling the light from the bottom QCL laser facet to a visible camera and mercury−cadmium−telluride (MCT) detector allowing simultaneously for one to view the bottom facet of the laser and focus the beam of the QCL onto the MCT detector. The signal from the MCT detector goes through a bias tee and LNA before being recorded on an RF spectrum analyzer. The experiment allows for polarization control, wavelength tunability, and power measurement.

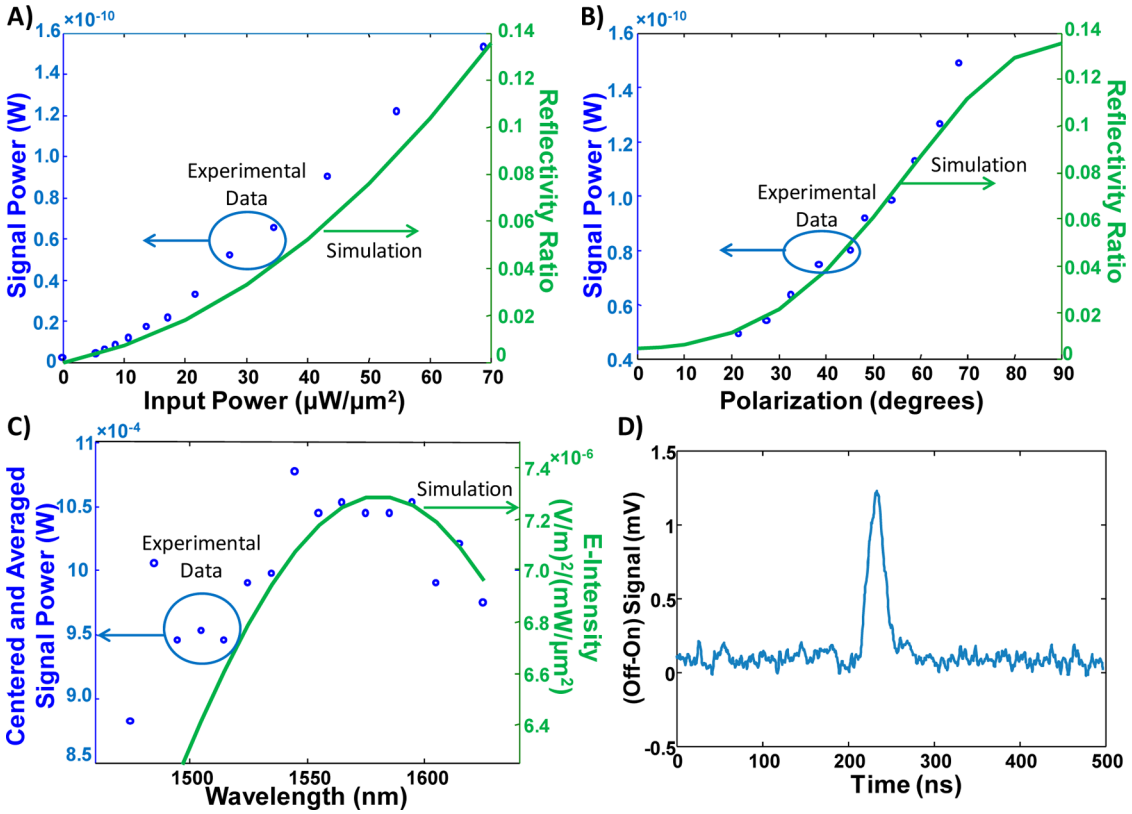

Figure 3. (A) Sideband power versus power of 1550 nm modulation signal. Left axis shows experimental signal power, and right axis shows simulation data. Experimental signal power (left axis in a, b) is limited by duty cycle and total power output; also, it is reduced by the responsivity of MCT detector. (B) Sideband power versus polarization of 1550 nm modulation signal. Left axis shows experimental signal power, and right axis shows simulation data. (C) Sideband power versus wavelength of modulation signal. Data are centered and averaged over several measurements. Left axis shows experimental signal power, and right axis shows simulation data. (D) Time response of modulated signal, showing difference in [off] minus [on] states. The [off] nominal peak is near 8 mV, so depth of modulation is nearing 15%.

calculated (see reflected signal plotted in Figure 1c,d). The free carrier lifetime τ is considered as a fitting parameter in the equation $\Delta N = \Delta P = G\tau$, where ΔN and ΔP are the change in carrier concentrations and G is the generation rate,[23] to derive

dx.doi.org/10.1021/nl3007424 | Nano Lett. XXXX, XXX, XXX−XXX

the same depth of modulation as demonstrated in the experimental results, and we have found the lifetime to be ~15 ns. Carrier lifetime in Ge can vary drastically in the literature, from milliseconds in bulk Ge[24] to hundreds of nanoseconds for amorphous Si:Ge alloys[25] or even near microseconds for amorphous Ge[26,27] or ~5 ns for evaporated polycrystalline Ge.[28] We do however expect our experimentally determined lifetime to be on the lower end of this broad spectrum due to its amorphous nature, large surface to volume ratio, and presence of metal on the surface.

Figure 3a,b shows the good agreement this model achieves, with a single adjustable parameter—the carrier lifetime—compared to the measured experimental data. Figure 3a shows the depth of modulation versus input power while Figure 3b shows the depth of modulation versus switch beam polarization. Figure 3c shows good agreement with the frequency response of the small antenna and the final device with no adjustable parameter.

We have also done a detailed simulation of our multiple quantum well structure and calculated the absorption of the structure in the near-infrared (NIR) to rule out the possibility that the absorption in the NIR may be causing a change in the intensity of the output at 6.1 μm. These simulations do show absorption nearing 10^5 m^{-1}, however, only for wavelengths below 1.2 μm for TE polarization and 1.1 μm for TM polarization. At 1550 nm, the absorption for TE and TM polarization is on the order of 10^{-2} and 10^{-4} m^{-1}, respectively.

After designing, simulating, and optimizing our structure, we have fabricated the test structure on the facet of a quantum cascade laser. The quantum cascade laser used in the device is the same as the one used in ref 29 with injector. After cleaving, the laser was mounted on a c-mount and tested at each possible stage during fabrication. After initial testing, the laser facet was coated in an electron-beam evaporation chamber with layers of MgF_2/Ge with thicknesses of 100/80 nm. After this initial evaporation, the laser was again tested, and then focused ion beam milling (FIB) was used to mill out the isolated Ge rectangle on which the smaller bowtie antenna would eventually sit. Next, the laser was again tested, and then another e-beam evaporation was done to deposit an aluminum layer (80 nm as in the simulation). After retesting the laser, the final antenna structure was milled out of the aluminum using a two-step process in FIB: first, the smaller antenna aligned to the germanium rectangle was milled using a low current (9.7 pA), and then the large antenna was aligned to the smaller antenna and milled at a high current (93 pA). The final antenna design is shown in Figure 1a,b.

After fabrication, our sample was experimentally tested in a two-way microscope setup, schematically pictured in Figure 2. From the top of the setup, there is an NIR camera allowing one to view the laser facet as well as simultaneously focus the modulation (1550 nm wavelength) laser light onto the laser facet. From the bottom of the setup, there is a broadband inverted microscope coupling the light from the laser facet to a visible camera and mercury−cadmium−telluride (MCT) detector allowing simultaneously for one to view the bottom facet of the laser and focus the beam of the QCL onto the MCT detector. We first observed the signal from the MCT detector on the oscilloscope with the 1550 nm source off and recorded its signal. Subsequently, we turned the 1550 nm source on and recorded the output of the MCT detector on the oscilloscope. When the 1550 nm source is on, there is a nearly 15% decrease in the peak signal of the QCL output (Figure 3d).

We have further characterized the device through a sideband measurement method by modulating the 1550 nm laser at 200 Hz and recording the output of the MCT detector in an RF spectrum analyzer. As the QCL is operating in pulsed mode at 0.5% duty cycle (103 kHz, 50 ns pulse width), we observe a main peak at 103 kHz, and when the 1550 nm laser is on, two sidebands at ±200 Hz with respect to the main peak. We have recorded the amplitude of the signal in dBm on the spectrum analyzer and converted it to a linear scale in Watts to observe the effect of the 1550 nm light on the modulation of the mid-infrared output of the QCL. We have varied the 1550 nm switch beam laser power and measured the output depth of modulation and plotted the result in Figure 3a. It can be found through the Drude model that $\varepsilon_{6.1} \propto I_{1.55}{}^2$, where $\varepsilon_{6.1}$ is the permittivity at 6.1 μm and $I_{1.55}$ is the light intensity at 1.55 μm. Using the above relation in our FDTD simulation, we observe a quadratic relationship between depth of modulation and $I_{1.55}$. This is in good agreement with experimental data (Figure 3a). We have also varied the polarization of the switch beam at 1550 nm. Figure 3b shows a good agreement between the measured power and the expected $\sin^2\theta$ relationship (where θ is the angle between the incident electric field and the long axis of the larger bow-tie as shown in Figure 1a). This is due to the cross-polarization relationship between the incoming switch beam and the smaller resonant bowtie polarization axis. We believe that the nonzero experimental signal observed at 0° polarization is due to experimental artifacts, such as imperfect shape of the bowtie (different from simulation), surface roughness at all interfaces, and imperfect alignment, all which could create plasmonic enhancement greater than zero at 0° polarization. Finally, we have varied the switch beam wavelength around 1550 nm and recorded the output depth of modulation (Figure 3c). On the right axis we have plotted the intensity enhancement of the smaller bowtie because the resonance of the smaller bowtie is the main factor in the frequency response of the device. The simulation and experimental data agree well, both peaking near 1580 nm. Figure 3d shows the difference signal on the oscilloscope when the switch beam is switched on. A difference in magnitude of 1.25 mV is obtained, in reference to a "before" signal of ~8 mV. This accounts for a depth of modulation of ~15%, with an input switch power of 70 μW/μm^2. The length of the pulse is ~50 ns, which is limited by heating in the laser core that is operated at 103 kHz for a 0.5% duty cycle. In Figure 3a,b, the power of modulation (left axis) is partly limited by the duty cycle and total power output of the QCL; it is also limited by the responsivity of the MCT detector used in the setup.

We have considered different recombination mechanisms that are proportional to first, second, and third powers of free carrier density[30] (for example, Shockley−Read−Hall, radiative, and Auger recombination). In bulk single-crystal germanium, the linear term is dominant up to carrier densities of $N \sim 0.5 \times 10^{19}$ cm^{-3}.[24] Therefore, we first assumed the linear term is dominant in our experiment and calculated the density that fits our experimental results. The resulted value is about 1×10^{19} cm^{-3} at a carrier lifetime of about 15 ns. Considering the large surface effect in our submicrometer Ge piece, and the fact that it is amorphous, we think the linear term is certainly dominant. It also produces a very good fit to our experimental data (see Figure 3).

We have observed a maximum modulation depth of ~15% at the maximum power of 70 μW/μm^2. This results in a switching energy of 8.4 pJ, in line with other all-optical switches.[12,13] One

dx.doi.org/10.1021/nl3007424 | Nano Lett. XXXX, XXX, XXX−XXX

way to improve the modulation depth would be to use a pulsed laser, which would allow for a higher carrier density. Lastly, by reducing the volume of the germanium to cover only the volume beneath the smaller bowtie hotspot, instead of the entire area below the smaller bowtie, we could increase the depth of modulation. By doing this, it would create a higher carrier density because the carriers would have less volume to diffuse over and the loss would increase, which would increase the change in the optical properties of the larger antenna when switched.

In conclusion, we have designed, simulated, fabricated, and experimentally characterized a quantum cascade laser with an integrated nonlinear optical antenna, which is switchable via a telecommunications wavelength laser. This device shows a viable optical method to modulate the far field of a laser through a near field interaction. We have characterized the device for optical power, polarization, and wavelength dependence. We have determined that the effect is not due to absorption in the quantum wells. Because of the wide-ranging usefulness for terahertz and short-wave infrared laser modulators, we believe such a device could be very useful in many applications from telecommunications[31] and free space communications[32] to range finding.[33]

AUTHOR INFORMATION

Corresponding Author

*E-mail: hmohseni@ece.northwestern.edu.

Notes

The authors declare no competing financial interest.

ACKNOWLEDGMENTS

The authors thank projects CBET-0932611 and EECS-0621887 under the National Science Foundation (NSF) and project W911NF-11-1-0390 under the Army Research Office (ARO). We are also grateful to the Materials Processing and Crystal Growth Facility and NUANCE facility at Northwestern University for fabrication and SEM characterizations.

REFERENCES

(1) Raether, H. *Surface Plasmons on Smooth and Rough Surfaces and on Gratings*; Springer: New York, 1988.

(2) Lassiter, J. B.; Aizpurua, J.; Hernandez, L. I.; Brandl, D. W.; Romero, I.; Lal, S.; Hafner, J. H.; Nordlander, P.; Halas, N. J. *Nano Lett.* **2008**, *8* (4), 1212−1218.

(3) Merlein, J.; Kahl, M.; Zuschlag, A.; Sell, A.; Halm, A.; Boneberg, J.; Leiderer, P.; Leitenstorfer, A.; Bratschitsch, R. *Nat. Photonics* **2008**, *2* (4), 230−233.

(4) Venkatram, N.; Kumar, R. S. S.; Rao, D. N.; Medda, S. K.; De, S.; De, G. *J. Nanosci. Nanotechnol.* **2006**, *6* (7), 1990−1994.

(5) Wu, W.; Bonakdar, A.; Mohseni, H. *Appl. Phys. Lett.* **2010**, *96*, 16.

(6) Ebbesen, T. W.; Lezec, H. J.; Ghaemi, H. F.; Thio, T.; Wolff, P. A. *Nature* **1998**, *391* (6668), 667−669.

(7) Gelfand, R. M.; Bruderer, L.; Mohseni, H. *Opt. Lett.* **2009**, *34* (7), 1087−1089.

(8) Righini, M.; Ghenuche, P.; Cherukulappurath, S.; Myroshnychenko, V.; de Abajo, F. J. G.; Quidant, R. *Nano Lett.* **2009**, *9* (10), 3387−3391.

(9) Kohoutek, J.; Dey, D.; Bonakdar, A.; Gelfand, R.; Sklar, A.; Memis, O. G.; Mohseni, H. *Nano Lett.* **2011**, *11* (8), 3378−82.

(10) Volpe, G.; Quidant, R.; Badenes, G.; Petrov, D. *Phys. Rev. Lett.* **2006**, *96*, 23.

(11) Dionne, J. A.; Diest, K.; Sweatlock, L. A.; Atwater, H. A. *Nano Lett.* **2009**, *9* (2), 897−902.

(12) Pala, R. A.; Shimizu, K. T.; Melosh, N. A.; Brongersma, M. L. *Nano Lett.* **2008**, *8* (5), 1506−1510.

(13) Large, N.; Abb, M.; Aizpurua, J.; Muskens, O. L. *Nano Lett.* **2010**, *10* (5), 1741−1746.

(14) Faist, J.; Capasso, F.; Sivco, D. L.; Sirtori, C.; Hutchinson, A. L.; Cho, A. Y. *Science* **1994**, *264* (5158), 553−556.

(15) Liu, H. C.; Capasso, F. *Intersubband Transitions in Quantum Wells: Physics and Device Applications II*; Academic Press: San Diego, 2000.

(16) Yu, N.; Cubukcu, E.; Diehl, L.; Belkin, M. A.; Crozier, K. B.; Capasso, F.; Bour, D.; Corzine, S.; Hofler, G. *Appl. Phys. Lett.* **2007**, *91*, 17.

(17) Yu, N.; Cubukcu, E.; Diehl, L.; Bour, D.; Corzine, S.; Zhu, J.; Hoefler, G.; Crozier, K. B.; Capasso, F. *Opt. Express* **2007**, *15* (20), 13272−13281.

(18) Dey, D.; Kohoutek, J.; Gelfand, R. M.; Bonakdar, A.; Mohseni, H. *Opt. Lett.* **2010**, *35* (16), 2783−2785.

(19) Dey, D.; Kohoutek, J.; Gelfand, R. M.; Bonakdar, A.; Mohseni, H. *IEEE Photonics Technol. Lett.* **2010**, *22* (21), 1580−1582.

(20) Tonouchi, M. *Nat. Photonics* **2007**, *1* (2), 97−105.

(21) Yu, N.; Blanchard, R.; Fan, J.; Wang, Q. J.; Pfluegl, C.; Diehl, L.; Edamura, T.; Furuta, S.; Yamanishi, M.; Kan, H.; Capasso, F. *IEEE Trans. Nanotechnol.* **2010**, *9* (1), 11−29.

(22) Palik, D. *Handbook of Optical Constants of Solids*; Academic: New York, 1985; Vol. *1*.

(23) Ashcroft, N. W.; Mermin, N. D. *Solid State Physics*; Brooks Cole: Salt Lake City, UT, 1976.

(24) Levinshteĭn, M. E.; Rumyantsev, S. L.; Shur, M. *Handbook Series on Semiconductor Parameters: Si, Ge, C (Diamond), GaAs, GaP, GaSb, InAs, InP, InSb*; World Scientific: Singapore, 1996.

(25) Shen, D. S.; Conde, J. P.; Chu, V.; Wagner, S. *J. Appl. Phys.* **1994**, *75* (11), 7349−7355.

(26) Watakabe, H.; Sameshima, T.; Kanno, H.; Miyao, M. *Thin Solid Films* **2006**, *508* (1−2), 315−317.

(27) Ishii, S.; Kurihara, M.; Aoki, T.; Shimakawa, K.; Singh, J. *J. Non-Cryst. Solids* **2000**, *266*, 721−725.

(28) Colace, L.; Masini, G.; Assanto, G. *IEEE J. Quantum Electron.* **1999**, *35* (12), 1843−1852.

(29) Dey, D.; Wu, W.; Memis, O. G.; Mohseni, H. *Appl. Phys. Lett.* **2009**, *94*, 8.

(30) Drumm, J. O.; Vogelgesang, B.; Hoffmann, G.; Schwender, C.; Herhammer, N.; Fouckhardt, H. *Semicond. Sci. Technol.* **2002**, *17* (10), 1115−1122.

(31) Hunter, D. K.; Smith, D. G. *J. Lightwave Technol.* **1993**, *11* (3), 495−511.

(32) Boffi, P.; Piccinin, D.; Mottarella, D.; Martinelli, M. *Opt. Commun.* **2000**, *181* (1−3), 79−88.

(33) Ruotsalainen, T.; Palojarvi, P.; Kostamovaara, J. *IEEE J. Solid-State Circuits* **2001**, *36* (8), 1228−1238.